Synsint Research Group

Available online at www.synsint.com

Synthesis and Sintering

ISSN 2564-0186 (Print), **ISSN** 2564-0194 (Online)

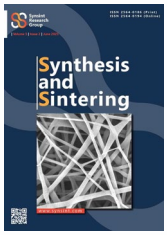

Research article

Physical properties of spin-coated nanocrystalline zinc oxide thin film

Omid Khanali, Khanali Nekouee *

Faculty of Materials and Manufacturing Technologies, Malek Ashtar University of Technology, Tehran, Iran

ABSTRACT

ZnO, in its wurtzite structure, is a widely studied metal oxide due to its unique optical and electronic properties, including efficient excitonic emission at room temperature. Zinc oxide thin films were synthesized through the dehydration of various precursors. In ethanol and mono-ethanolamine, zinc acetate (I) and zinc nitrate (II) were dissolved. Glass substrates were coated using the sol-gel spin coating method (3000 rpm for 10 s), followed by heating at 250 °C. This process was done five times to make the films thicker (and allow them to form five layers on the substrate), and then they were annealed at 450 °C for 3 hours in air, yielding 200 nm-thick films. Where acetate-derived ZnO demonstrated superior performance: 92% optical transmission at 1100 nm (vs. 80% for nitrate), a widened bandgap (3.3 eV), and enlarged crystallite size (74 nm), attributed to reduced defect density and homogeneous morphology. The presence of various vibration modes in the prepared samples was also revealed by Raman spectroscopy (RS) of the annealed films. The presence of concentrated stresses within the coated films is also determined using RS, and the scanning electron microscopy results confirm the Raman E_2 peaks by FE-SEM images.

KEYWORDS

Thin films
Zinc oxide
Band gap
Sol-gel
Spin coating

OPEN ACCESS

1. Introduction

Zinc oxide (ZnO) is a direct band gap semiconductor with a wide band gap of 3.3 eV. ZnO, in its wurtzite structure, is a widely studied metal oxide due to its unique optical and electronic properties, including efficient excitonic emission at room temperature. It has been extensively used in optics, biomedical sciences, energy applications, optoelectronic sensors, actuators, transistors, and solar cells [1–3].

Techniques for fabricating textured ZnO thin films on a substrate include pulsed laser deposition, sputtering, molecular-beam epitaxy, chemical vapour deposition, sol-gel methods, and others [4–8]. Nanostructured ZnO films respond particularly well to the sol-gel spin coating technique. Sol-gel deposition allows for large-area coatings with excellent optical properties and enables the fabrication of multi-component oxide layers on glass substrates [9]. Furthermore, the green coating characterization was easily controlled, and a large fabrication area of thin films was achieved. Over the years, researchers have refined the sol-gel spin coating method to achieve better control over the properties of the deposited thin films[10, 11].

Kim et al. [12] examined the influence of pre-heating temperature on a zinc acetate (ZnAc), isopropanol, and monoethanolamine (MEA) solution, employing a range of temperatures for a ten-minute pre-heat duration. Separately, Balta et al. [13] investigated the effect of precursor concentration on the crystal structure of ZnO thin films. Their synthesis, using varying molar concentrations of zinc acetate dihydrate, yielded films exhibiting a hexagonal wurtzite structure after annealing at 600 °C, as confirmed by X-ray diffraction (XRD) analysis. This study investigates the physical properties of ZnO thin films prepared through sol-gel spin coating. This study investigates the synthesis process, characterization techniques, and the impact of different precursor solutions on the crystallization and quality of

* Corresponding author. *E-mail address:* khnekouee @gmail.com (K. Nekouee)

Received 19 January 2025; Received in revised form 5 April 2025; Accepted 19 April 2025.

https://doi.org/10.53063/synsint.2025.52268

ZnO thin films. Additionally, we will discuss the structural, morphological, optical, and stress-related properties of the ZnO thin films [13].

2. Experimental procedures

2.1. Materials and processing

Sol-gel processing was used to create nanocrystalline pure zinc oxide films from two different precursor solutions of zinc acetate (I) (Merck, Germany) and zinc nitrate (II) (Merck, Germany). The use of two different precursor materials was based on the fact that ZnO particles derived from an initially homogeneous solution are sensitive to solution conditions. In a homogeneous solution, particle growth includes three basic stages: nucleation, growth from dissolved species, and then net movement of species between and by existing particles. The precursor materials were dissolved in a mixture of absolute Ethanol (Merck, Germany) and mono-ethanolamine (MEA) at a concentration of 0.50 mol/l (Merck, Germany). MEA served as both a base and a complexing agent. MEA to zinc acetate (I) and zinc nitrate (II) molar ratios were set to 1. For 1 hour, the prepared solution was stirred with a magnetic stirrer at 70 °C. Before deposition, the glass substrates were cleaned with acetone to remove surface contaminants and thoroughly rinsed with deionized water. Sol-gel spin coating (3000 rpm for 10 seconds) was used to deposit this solution on glass substrates (Fig. 1). To consolidate the deposited material after each step, the samples were partially preheated at 250 °C for 15 minutes. This method was repeated several times to thicken the films and allow them to form five layers. The multi-layered thin films were annealed at 450 °C for 3 hours in an air atmosphere to obtain fully crystallized films and to remove organic residues. The flow chart of the sol-gel spin coating technique for the preparation of the ZnO thin film is shown in Fig. 1 [14, 15].

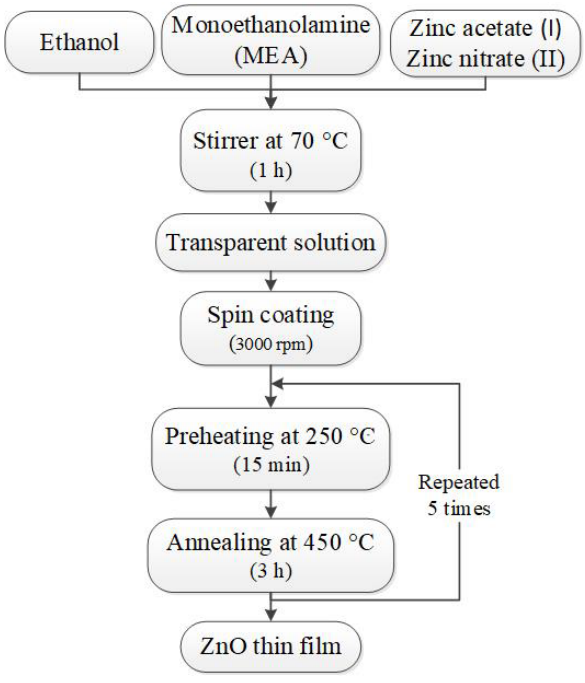

Fig. 1. Flow chart of sol-gel spin coating procedure for preparation of the ZnO thin films.

2.2. ZnO films characterization

The crystalline phase of the ZnO thin films was characterized by an X-ray diffractometer (XRD, Siemens D-500) using CuKα radiation (40 kV, 30 mA) at a scanning rate of 2 °/min. The morphologies were observed by a field emission scanning electron microscope (FE-SEM) (MIRA3, TE-scan, Czech Republic) with an operating voltage of 10 kV. The surface topography was also observed by an AFM operating in the tapping mode (AFM, model Nano-surf Mobile, S Instruments Switzerland). The scan area for AFM measurements was 5 μm × 5 μm, which was selected to provide a representative analysis of the surface morphology and roughness of the ZnO films while ensuring high-resolution imaging of the sample features.

The transmission spectra of the films were measured by a double-beam ultraviolet/visible (UV-4100) spectrophotometer with a wavelength extended of 200–1100 nm, and the optical band gap was measured from the transmission spectra. For each experimental condition, five measurements were taken per sample, and four samples were analyzed to ensure statistical reliability. The results were then averaged to provide the final values. To determine the band gap of the ZnO films, UV-Vis spectroscopy and Tauc's plot were employed. By plotting $(\alpha h\nu)^2$ versus photon energy ($h\nu$) and extrapolating the linear region of the curve, the direct band gap was calculated.

Raman spectra were measured within the visible light utilizing 514.5 nm excitation lines from an argon ion laser and a DILOR XY spectrometer in the backscattering geometry (equipped with a liquid nitrogen cooled CCD Jobin Yvon Detector). The incident laser power was limited to ~2 mW to prevent excessive sample heating. The integration time was set to 10–30 seconds, and the spectral resolution was 2–4 cm^{-1}, ensuring accurate resolution of the Raman peaks while maintaining a high signal-to-noise ratio. [16, 17].

3. Results and discussion

3.1. Crystal structure of zinc oxide

ZnO crystallizes in hexagonal Wurtzite or cubic zinc blend structure. The Structure includes sp^3 covalent bonding. Wurtzite is the structure that is thermodynamically stable under the surrounding conditions. Fig. 2 illustrates the crystal structure of zinc oxide (ZnO) in different orientations, highlighting its atomic arrangement and key characteristics. As shown in Fig. 2a, ZnO adopts a hexagonal wurtzite structure with alternating zinc (Zn) and oxygen (O) layers along the c-axis, which is its most stable phase under ambient conditions. The unit cell reveals strong Zn–O bonds that contribute to its structural stability. Fig. 2b presents a closer view of the layered arrangement, where strong in-plane Zn–O bonds and weaker interlayer interactions are evident. This layered structure is further emphasized in Fig. 2c, showcasing ZnO's potential as a three-dimensional (3D) material with enhanced optical, piezoelectric, and semiconductor properties, making it suitable for various electronic and sensing applications [18].

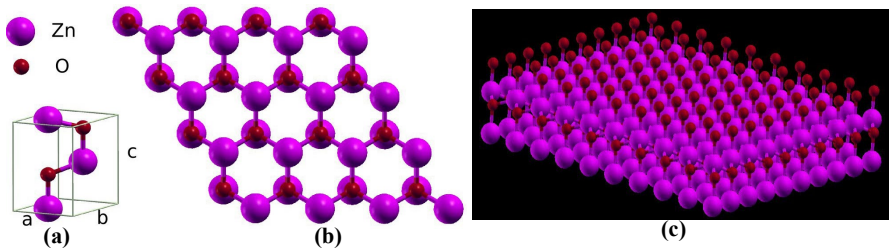

Fig. 2. Bulk crystal structure of wurtzite zinc-oxide with bulk lattice parameters of a = 3.25 Å, b = 0.38 Å, and c = 5.21 Å in different forms, a) one-dimensional, b) two-dimensional, and c) three-dimensional.

The XRD spectra of annealed ZnO thin films on the glass substrate in Fig. 3 show that the peaks agree well with those from the Joint Committee on Powder Diffraction Standards (JCPDS) card file data for ZnO powder. Both samples' XRD patterns revealed high crystallinity of the ZnO thin film structure. All of the films had a hexagonal crystallographic phase, with the (002) and (101) planes being the most preferred orientations for zinc acetate (I) and zinc nitrate (II) respectively. A high degree of special orientation (with the c-axis perpendicular to the substrate) and small traces from the peaks of (100) and (101) planes were also observed for zinc acetate (I) derived one [19, 20]. The presence of broad diffraction peaks confirmed that the particles are on the nanometric scale. Other than ZnO peaks, no other characteristic peaks were observed (as the glass substrate has no peaks due to its amorphous structure). Many groups have reported similar findings [21, 22]. The crystallite size (D) of the samples is also determined utilizing Scherer's formula of which is as follows:

$$D = \frac{K\lambda}{\beta \cos(\theta)} \quad (1)$$

where K is the Scherrer constant (taken as 0.94 for spherical crystallites), λ is the X-ray wavelength (1.5406 Å, Cu Kα radiation), β is the full width at half maxima (FWHM), and θ is the Bragg's angle. The intensity along (100), (002), and (101) planes is sharply increased with different precursors. The crystallite sizes for the ZnO crystal have been shown in Table 1.

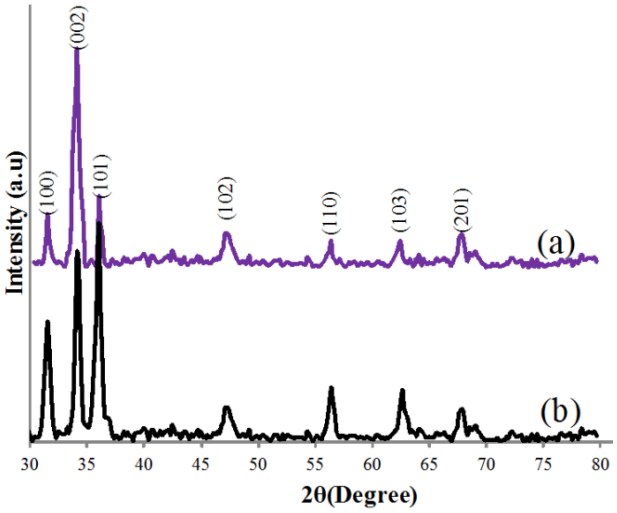

Fig. 3. XRD patterns of the ZnO thin film prepared by: a) zinc acetate (I) and b) zinc nitrate (II) precursors.

3.2. FE-SEM and cross section images

Fig. 4 shows FE-SEM micrographs of ZnO thin films produced using zinc acetate (I) and zinc nitrate (II) as precursor materials. The surface morphologies of the ZnO thin films were completely different, as shown in Fig. 4. Fig. 4a depicts the surface morphology of ZnO thin films prepared with zinc acetate (I) as a precursor. This FE-SEM image shows that the aligned hexagonal ZnO microstructures were grown nearly uniformly on a large scale, with the requested ZnO microstructures having a diameter of around 2μm. According to the XRD pattern, ZnO microstructures grew preferentially along the (002) plane because the hexagonal column spaghettis were regular and nearly perpendicular to the substrate. Znaidi et al. [23] observed similar types of square slabs in ZnO thin films. A persistent thin film could be observed with stronger particle-particle interaction and stronger particle-substrate interaction. The FE-SEM image of the thin film obtained by using zinc nitrate (II) as the precursor is shown in Fig. 4b. The image clearly shows a non-uniform surface morphology and indefinite non definite grain boundaries. The partially hexagonal crystal islands on the generally flat seeding layer were also noted. Because of their hexagonal appearance, these islands (small square shape) can be explained as ZnO crystal seeds. This result suggests that the seeding layer and seeding crystals were made of unsymmetrically oriented ZnO crystals, which was also confirmed by XRD analysis [24, 25].

Fig. 5 shows FE-SEM micrographs of cross-sections perpendicular to the ZnO thin film of various precursor materials. Each image clearly shows the locations corresponding to the film and substrate. The thicknesses of the films were measured using FE-SEM micrographs with resolutions ranging from 100 to 200 nm. The deposition process was carried out in five steps, with each step depositing approximately

Table 1. Obtained data from the XRD pattern.

Sample	2θ (deg)	hkl	FWHM	Crystal size (nm)
Zinc acetate (I)	31.50	(100)	0.0864	96
	34.11	(002)	0.1246	64
	36.046	(101)	0.1246	64
				Avg.=74.6
Zinc nitrate (II)	31.51	(101)	0.048	172
	34.11	(112)	0.072	115
	36.0465	(211)	0.072	115
				Avg.=134

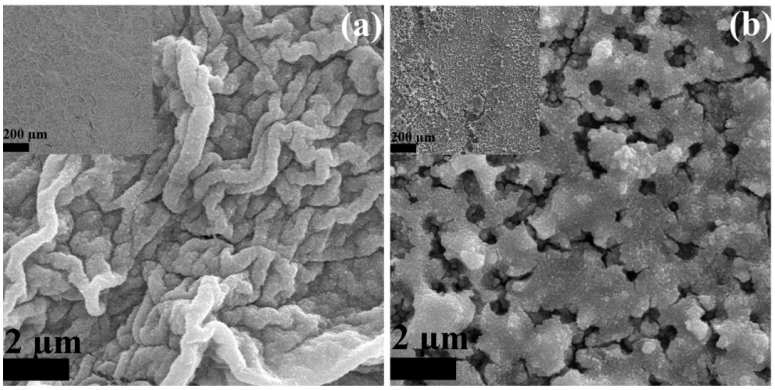

Fig. 4. FE-SEM micrographs of the surface of ZnO nanocrystalline coatings prepared by: a) zinc acetate (I) and b) zinc nitrate (II) precursors.

nanometers onto the glass substrate to achieve a total thickness of 200 nm. FE-SEM micrographs prepared with zinc acetate (I) precursor are shown in Fig. 5a. Micro-spaghettis and dense formation of ZnO thin films can be seen. The porosity of ZnO films in Fig. 5b, prepared by the zinc nitrate (II) precursor, shows that the ZnO grains have completely separated from each other and formed crystal islands on the relatively flat shapes [12, 26].

3.3. Roughness investigations by AFM

The surface roughness of the ZnO thin films was measured using an AFM. Each sample had its root mean square roughness (RMS/Rq) and average roughness (Ra) measured. Fig. 6 depicts three-dimensional AFM images of zinc acetate (I) and zinc nitrate (II). The sample's surface roughness was calculated using an image size of 8×8 μm^2. Ra values for zinc acetate (I) and zinc nitrate (II) as precursor materials were 85 nm and 116 nm, respectively, according to AFM data. Furthermore, the roughness analysis yielded Rq heights of 92 and 144.16 nm, respectively. The use of zinc acetate (I) as a precursor reduces the roughness of the surface [27–29].

3.4. Optical characteristics

Fig. 7 depicts the optical transmittance spectrum of ZnO thin films with various precursor materials over a wavelength range of 200 to 1100 nm. The sharp absorption peaks for zinc acetate (I) and zinc nitrate (II) are around 385 and 375 nm, respectively. The optical absorption at the absorption edge corresponds to the transition from the valence band to the conduction band, whereas absorption in the visible region is related to some local energy levels created by inherent defects. Chemical reactions in different precursor materials could explain the varying sharp absorption and optical transmission. Optical transmission is greatest at 1100 nm, with 92% and 80% for zinc acetate (I) and zinc nitrate (II), respectively. This decrease in optical transmission could be explained by the formation of structure defects during chemical reactions, which could result in the zinc nitrate (II) precursor material having more defects in thin films than the zinc acetate (I) precursor material [30].

To calculate the optical band gap of the ZnO films, the adsorption coefficient of the film (α) was determined from the thickness of the film and its transmittance with Eq. 2:

$$\alpha = \frac{1}{D}\ln\left(\frac{1}{T}\right) \tag{2}$$

where D and T are the thickness of the film and its transmittance, respectively. The thickness of the film was calculated through averaging many cross-section FE-SEM micrographs of the ZnO films (Fig. 6). Thicknesses of 180 nm and 200 nm were determined for the thin films of the zinc acetate (I) and the zinc nitrate (II) precursor

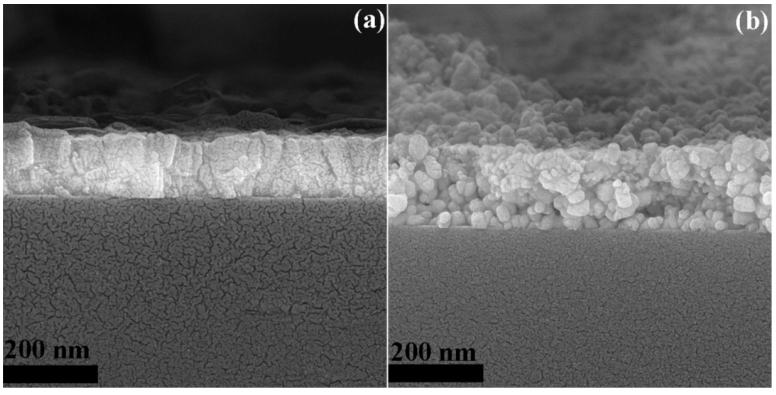

Fig. 5. Cross-section view of the FESEM of the ZnO films prepared by: a) zinc acetate (I) and b) zinc nitrate (II) precursors.

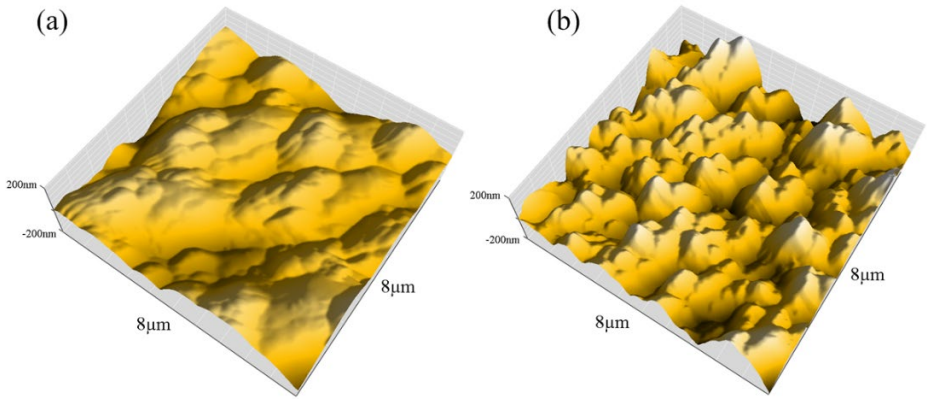

Fig. 6. Three-dimensional AFM images of the ZnO nanocrystalline coatings prepared by: a) the zinc acetate (I) and b) the zinc nitrate (II) precursors.

materials, respectively. For the direct band transition, the optical band gap of the films could be calculated by analysing the relationship between photon energy (hν) and absorption coefficient (α) with the following formula:

$$(\alpha h\nu)^2 = A(h\nu - E_g) \quad (3)$$

where A is a constant, hν is the photon energy, and E_g is the optical band gap. The optical band gap (E_g) was calculated by extrapolating the linear portion of the $(\alpha h\nu)^2$ versus the hν graph to intersect the energy axis at α=zero. Fig. 8 shows the $(\alpha h\nu)^2$ versus hν (eV) for the ZnO film prepared by the different precursor materials [31].

The measured optical band gap values were in the range of 3.3 and 3.2 eV for the ZnO films prepared by the zinc acetate (I) and the zinc nitrate (II) precursor materials respectively, which is very close to the band gap of the inherent ZnO bulk material and are in accordance with the previous literature reports [32]. Also, it is a current phenomenon in direct band gap semiconductors [33, 34].

3.5. Raman spectroscopy

Fig. 9 illustrates the Raman spectra of the thin films prepared by the zinc acetate (I) and zinc nitrate (II). The spectra were normalized about the main peak at 434 cm^{-1} in the bulk ZnO material. Table 2 reports data on the mode frequencies of the ZnO crystal from many Research studies and our results. The frequencies from the E_2^{high}, A_1 (LO), and E_1 (LO) modes are Raman prepared by the different precursor materials. E_2^{high} vibration is a feature of the wurtzite phase [29].

Fig. 9a shows the Raman spectra of the zinc acetate (I) thin films. Raman spectra have mode E_2^{high} = 434 cm^{-1}, A_1 (LO) = 562 cm^{-1}. The peak A_1 (LO) is approximately attributable to the formation of defects and impurities in the thin films. Thin films had a high quality of the wurtzite structure, because of the high intensity of E_2^{high} than A_1 (LO).

Stress in the wurtzite structure crystals impacts the E_2^{high} phonon frequency. An increase in the E_2^{high} phonon frequency is attributed to compressive stress, whilst a decline in the E_2^{high} phonon frequency is attributed to tensile stress. Thus, Raman spectroscopy of the E_2^{high} phonon is a method to determine residual stress within ZnO crystallized films. On the other hand, the stress is due to the mismatch of the thermal expansion coefficient of the ZnO thin films (4.75×10^{-6} K^{-1}) and the glass substrates (Si: 2.6×10^{-6} K^{-1}).

Fig. 9b shows the Raman spectra of the zinc nitrate (II) thin films. Raman spectra shown modes E_2^{high} = 422 cm^{-1}, E_1 (LO) =561 cm^{-1}.

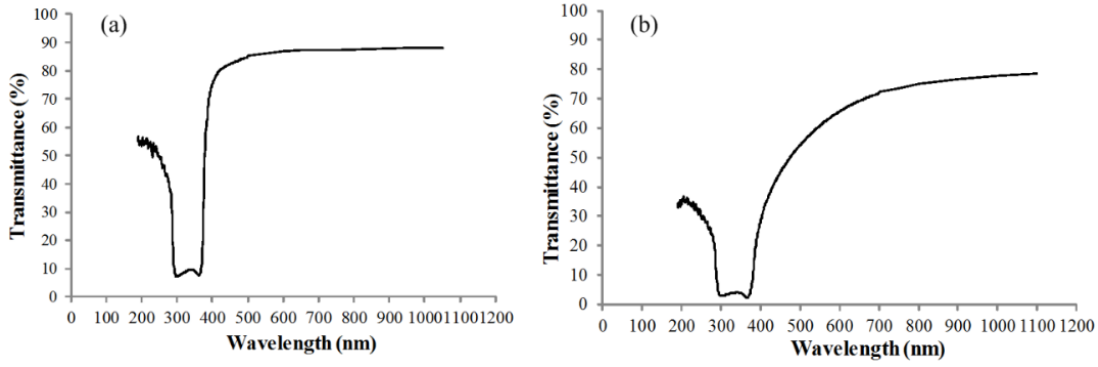

Fig. 7. The optical transmittance spectrum of the ZnO films prepared by: a) zinc acetate (I) and b) zinc nitrate (II) precursors.

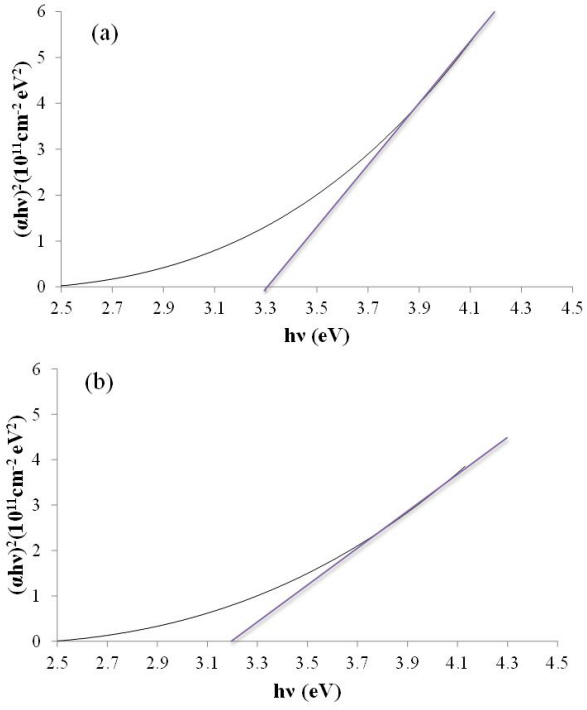

Fig. 8. $(\alpha h\nu)^2$ versus the hν for the ZnO films prepared by: a) the zinc acetate (I) and b) the zinc nitrate (II) precursors.

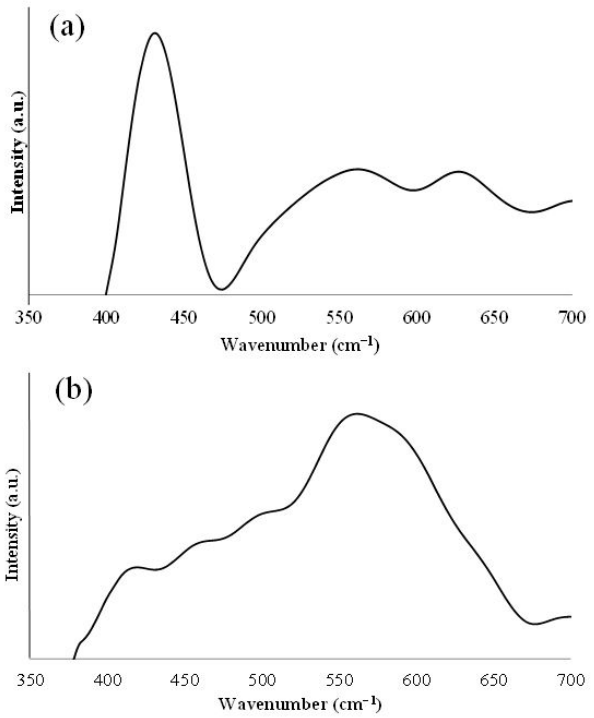

Fig. 9. Raman spectra of glass substrate, ZnO thin films prepared by: a) zinc acetate (I) and b) zinc nitrate (II) precursors.

The peak E_2^{high} as A_1 (LO) is approximately attributable to the formation of defects and impurities in the thin films. The thin films don't have a high quality of the wurtsite structure, because of the too low intensity of E_2^{high} than E_1 (LO).

The peak E_1 (LO) for the ZnO thin film produced via zinc nitrate (II), nearly positioned at 561 cm^{-1}, which is attributable to the formation of defects such as an absence of oxygen, interstitial Zn, and the free carriers. The displacement changes of this peak, annealing without controlled atmosphere, however, suggest a relatively low density of defects in these coatings.

The behaviour of the Raman peak of E_2^{high} is confirmed by FE-SEM images (Fig. 4). In this case, the frequency E_2^{high} is lower than its bulk material, and 437 cm^{-1} is a shift towards lower frequencies, as has been reported. The film has tensile stress and compression strain.

Table 2. Experimental data of the frequencies (cm^{-1}) of the ZnO thin film and ZnO bulk material.

Mode	ZnO thin film zinc acetate (I)	ZnO thin film zinc nitrate (II)	ZnO crystal (cm^{-1})	ZnO crystal (cm^{-1})
E_2^{high}	434	422	439	444
A_1 (LO)	562	-	574	579
E_1 (LO)	-	561	580	591

4. Conclusions

The ZnO thin films were created by dehydrating various precursor materials such as zinc acetate (I) and zinc nitrate (II), which were then dissolved in ethanol and mono-ethanolamine (MEA). The solutions were applied to glass using the sol-gel spin-coating technique. After a preheating treatment at 250 °C and a final thermal treatment at 450 °C, the thin films were crystallized into ZnO. The following results have been obtained:

- The films were transparent and homogenous and *c*-axis oriented. Successive deposition of the films was carried out to increase the thickness. The (002) orientation is modified for zinc acetate films.
- The AFM images indicate that ZnO thin films have been prepared by zinc acetate (I) material precursor, and it seems that by choosing this suitable precursor material, the grain size and roughness could be controlled.

Raman results of the ZnO thin films indicate the presence of stress concentrations within the structure of the films. The behavior of the peak E_2^{high} confirms the microcrystalline grain films, as the SEM study also proves these results. The Raman investigation of the sediment solution confirms that the ZnO bonds presumably play the role of the initiation of the crystallization during the treatment of the coatings.

CRediT authorship contribution statement

Omid Khanali: Conceptualization, Methodology, Writing – original draft.

Khanali Nekouee: Validation, Writing – review & editing, Supervision.

Data availability

The data underlying this article will be shared on reasonable request to the corresponding author.

Declaration of competing interest

The authors declare that they have no known competing financial interests or personal relationships that could have appeared to influence the work reported in this paper.
The authors declare the following financial interests/personal relationships, which may be considered as potential competing interests.

Funding and acknowledgment

The authors would like to thank INSF of Iran Contract Number of 97/sad/42699 on 9/11/2024 for complete financial support provided for this research work.

References

[1] M.A. Borysiewicz, ZnO as a functional material, a review, Crystals. 9 (2019) 505. https://doi.org/10.3390/cryst9100505.
[2] M.T. Noman, N. Amor, M. Petru, Synthesis and applications of ZnO nanostructures (ZONSs): A review, Crit. Rev. Solid State Mater. Sci. 47 (2022) 99–141. https://doi.org/10.1080/10408436.2021.1886041.
[3] D.K. Sharma, S. Shukla, K.K. Sharma, V. Kumar, A review on ZnO: Fundamental properties and applications, Mater. Today Proc. 49 (2022) 3028–3035. https://doi.org/10.1016/j.matpr.2020.10.238.
[4] P. Kumar, Nisha, P. Sarkar, S. Singh, B. Mishra, R.S. Katiyar, The influence of post-growth heat treatment on the optical properties of pulsed laser deposited ZnO thin films, Appl. Phys. A. 128 (2022) 372. https://doi.org/10.1007/s00339-022-05511-2.
[5] S. Flickyngerova, K. Shtereva, V. Stenova, D. Hasko, I. Novotny, et al., Structural and optical properties of sputtered ZnO thin films, Appl. Surf. Sci. 254 (2008) 3643–3647. https://doi.org/10.1016/S0040-6090(99)00060-7.
[6] M. Opel, S. Geprägs, M. Althammer, T. Brenninger, R. Gross, Laser molecular beam epitaxy of ZnO thin films and heterostructures, J. Phys. D: Appl. Phys. 47 (2013) 034002. https://doi.org/10.1088/0022-3727/47/3/034002.
[7] T.M. Barnes, J. Leaf, C. Fry, C.A. Wolden, Room temperature chemical vapor deposition of c-axis ZnO, J. Cryst. Growth. 274 (2005) 412–417. https://doi.org/10.1016/j.jcrysgro.2004.10.015.
[8] Y.-S. Ho, K.-Y. Lee, Fabrication of highly oriented (002) ZnO film on glass by sol–gel method, Thin Solid Films. 519 (2010) 1431–1434. https://doi.org/10.1016/j.tsf.2010.09.006.
[9] A. Abdel-Galil Farrag, M.R. Balboul, Nano ZnO thin films synthesis by sol–gel spin coating method as a transparent layer for solar cell applications, J. Sol-Gel Sci. Technol. 82 (2017) 269–279. https://doi.org/10.1007/s10971-016-4277-8.
[10] M.A. Shafi, A. Bouich, K. Fradi, J.M. Guaita, L. Khan, B. Mari, Effect of deposition cycles on the properties of ZnO thin films deposited by spin coating method for CZTS-based solar cells, Optik. 258 (2022) 168854. https://doi.org/10.1016/j.ijleo.2022.168854.
[11] R. Ebrahimifard, H. Abdizadeh, M.R. Golobostanfard, Controlling the extremely preferred orientation texturing of sol–gel derived ZnO thin films with sol and heat treatment parameters, J. Sol-Gel Sci. Technol. 93 (2020) 28–35. https://doi.org/10.1007/s10971-019-05157-2.
[12] Y.-S. Kim, W.-P. Tai, S.-J. Shu, Effect of preheating temperature on structural and optical properties of ZnO thin films by sol–gel process, Thin solid films. 491 (2005) 153–160. https://doi.org/10.1016/j.tsf.2005.06.013.
[13] A. Kaya Balta, Ö. Ertek, N. Eker, İ. Okur, MgO and ZnO composite thin films using the spin coating method on microscope glasses, Mater. Sci. Appl. 6 (2015) 40–47. https://doi.org/10.4236/msa.2015.61006.
[14] M. Ayachi, F. Ayad, A. Djelloul, S. Sali, S. Anas, et al., Investigation of structural, morphological, and optical properties of (Ni/Co, Fe/Co, and Fe/Ni) co-doped ZnO thin films prepared by sol-gel spin coating technique, J. Sol-Gel Sci. Technol. 110 (2024) 1–15. https://doi.org/10.1007/s10971-024-06376-y.
[15] I.Y. Bouderbala, A. Guessoum, S. Rabhi, O. Bouhlassa, I.-E. Bouras, Optical band-diagram, Urbach energy tails associated with photoluminescence emission in defected ZnO thin films deposited by sol–gel process dip-coating: effect of precursor concentration, Appl. Phys. A. 130 (2024) 205. https://doi.org/10.1007/s00339-024-07366-1.
[16] G. Demircan, E.F. Gurses, A. Acikgoz, S. Yalcin, B. Aktas, Effects of spin coating parameters on stress, electrical and optical properties of multilayer ZnO thin film prepared by sol–gel, Mol. Cryst. Liq. Cryst. 709 (2020) 61–69. https://doi.org/10.1080/15421406.2020.1816009.
[17] S. Handani, D. Dahlan, S. Arief, Enhanced structural, optical and morphological properties of ZnO thin film using green chemical approach, Vacuum. 179 (2020) 109513. https://doi.org/10.1016/j.vacuum.2020.109513.
[18] B.K. Dejene, T.M. Geletaw, A review of plant-mediated synthesis of zinc oxide nanoparticles for self-cleaning textiles, Res. J. Text. Appar. 28 (2024) 879–892. https://doi.org/10.1108/RJTA-12-2022-0154.
[19] N.S. Rao, M.B. Rao, Structural and optical investigation of ZnO nanopowders synthesized from zinc chloride and zinc nitrate, Am. J. Mater. Sci. 5 (2015) 66–68. https://doi.org/10.5923/j.materials.20150503.02.
[20] K. Nadarajah, C.Y. Chee, C.Y. Tan, Influence of annealing on properties of spray deposited ZnO thin films, J. Nanomater. 2013 (2013) 22–22. https://doi.org/10.1155/2013/146382.
[21] E. Heredia, C. Bojorge, J. Casanova, H. Cánepa, A. Craievich, G. Kellermann, Nanostructured ZnO thin films prepared by sol–gel spin-coating, Appl. Surf. Sci. 317 (2014) 19–25. https://doi.org/10.1016/j.apsusc.2014.08.046.
[22] D. Aryanto, E. Hastuti, M. Taspika, K. Anam, I. Isnaeni, et al., Characteristics and photocatalytic activity of highly c-axis-oriented ZnO thin films, J. Sol-Gel Sci. Technol. 96 (2020) 226–235. https://doi.org/10.1007/s10971-020-05361-5.
[23] L. Znaidi, Sol–gel-deposited ZnO thin films: A review, Mater. Sci. Eng: B. 174 (2010) 18–30. https://doi.org/10.1016/j.mseb.2010.07.001.
[24] G. Swati, S. Mishra, D. Yadav, R. Sharma, D. Dwivedi, et al., High yield synthesis and characterization of aqueous stable zinc oxide nanocrystals using various precursors, J. alloys compd. 571 (2013) 1–5. https://doi.org/10.1016/j.jallcom.2013.03.218.
[25] K.O. Olumurewa, M.A. Eleruja, Photoelectrical and thermal sensing measurement of spin coated ZnO and ZnO-RGO thin film, Phys. B: Cond. Matter. 650 (2023) 414588. https://doi.org/10.1016/j.physb.2022.414588.
[26] F. Zahedi, R. Sabet Dariani, S.M. Rozati, Spray Pyrolysis Deposition of ZnO Thin Films from Zinc Chloride Precursor Solution at Different Substrate Temperatures, Acta Metall. Sin. (Engl. Lett.). 28 (2015) 110–114. https://doi.org/10.1007/s40195-014-0177-5.
[27] S. Youssef, P. Combette, J. Podlecki, R.A. Asmar, A. Foucaran, Structural and optical characterization of ZnO thin films deposited by reactive rf magnetron sputtering, Cryst. Growth Des. 9 (2009) 1088–1094. https://doi.org/10.1021/cg800905e.
[28] J. Quiñones-Galván, I. Sandoval-Jiménez, H. Tototzintle-Huitle, L. Hernández-Hernández, F. de Moure-Flores, et al., Effect of precursor solution and annealing temperature on the physical properties of

Sol–Gel-deposited ZnO thin films, Results Phys. 3 (2013) 248–253. https://doi.org/10.1016/j.rinp.2013.11.001.
[29] L. Znaidi, T. Chauveau, A. Tallaire, F. Liu, M. Rahmani, et al., Textured ZnO thin films by sol–gel process: Synthesis and characterizations, Thin Solid Films. 617 (2016) 156–160. https://doi.org/10.1016/j.tsf.2015.12.031.
[30] R. Bekkari, B. Jaber, H. Labrim, M. Ouafi, N. Zayyoun, L. Laânab, Effect of solvents and stabilizer molar ratio on the growth orientation of sol-gel-derived ZnO thin films, Int. J. Photoenergy. 2019 (2019) 3164043. https://doi.org/10.1155/2019/3164043.
[31] T. Ivanova, A. Harizanova, T. Koutzarova, B. Vertruyen, Optical and structural properties of sol–gel derived ZnO: F thin films, AIP Conference Proceedings, AIP Publishing. 2075 (2019) 140005. https://doi.org/10.1063/1.5091320.
[32] H. Hartnagel, Semiconducting transparent thin films, CRC Press. (1995).
[33] M. Khan, K. Bhatti, R. Qindeel, N. Alonizan, H.S. Althobaiti, Characterizations of multilayer ZnO thin films deposited by sol-gel spin coating technique, Results Phys. 7 (2017) 651–655. https://doi.org/10.1016/j.rinp.2016.12.029.
[34] M.P. Gonullu, D.D. Cakil, C. Cetinkaya, Influence of thermal treatment and Fe doping on ZnO films by ultrasonic spray pyrolysis, Thin Solid Films. 793 (2024) 140265. https://doi.org/10.1016/j.tsf.2024.140265.